Int J Adv Manuf Technol (2017) 93:2021–2035
DOI 10.1007/s00170-017-0664-8

ORIGINAL ARTICLE

A new multi-vision-based reconstruction algorithm for tube inspection

Peng Jin[1] · **Jianhua Liu**[1] · **Shaoli Liu**[1] · **Xiao Wang**[1]

Received: 14 November 2016 / Accepted: 13 June 2017 / Published online: 26 June 2017

Abstract Complex tubes are used widely in aerospace vehicles today, and their accurate assembly can determine the equipment's performance and longevity. The machining precision of the tube determines its assembly reliability. As most tubes are metallic, springback is a major factor preventing them from realizing accuracy requirements in primary processing. Thus, it is important to inspect the processed tubes and then fix any geometric errors to satisfy the assembly requirements. However, the widely adopted tube inspection method in the literature is time-consuming and inconvenient because it is greatly dependent on human operation. In fact, there is no effective inspection method for tubes with complex shapes and large dimensions. To address this, an automatic tube reconstruction algorithm based on multi-vision is proposed in this paper. The algorithm discretizes the tube into many small cylinders, referred to as primitives. Multi-vision technology and the tube edges are then used to reconstruct the primitives to form the initial model, from which a three-dimensional model can be constructed within 2 min. Our algorithm dramatically improves the reconstruction speed because it concentrates only on the reconstruction of finite cylinders rather than point clouds on the tube surface. And the reconstruction accuracy is 0.17 mm, allowing arc recognition of bending angles ranging from 1° to 180°. Also, the restrictions due to reflection on the surface and the lack of necessary texture for matching are solved at the same time. A comparison of reconstructed and computer-aided design (CAD) models resolves geometric error and springback for machining parameter optimization, providing improved accuracy particularly for tube bending, which is of great significance for the realization of automated tube production.

Keywords Cylinder primitive · Multi-vision · Shape from silhouette · Tube reconstruction

1 Introduction

Complex tubes are widely used in aerospace applications and electromechanical products, whereby accurate assembly is critical to the products' reliability, performance, and life cycle [1]. With the miniaturization of complex electromechanical products [2], the requirement for tube assembly has increased significantly.

The reliability of the assembly is directly affected by the machining quality of tubes [1, 3]. As metallic bent tubular parts have attracted increasing applications, for any bending process, the complex uneven tension and compression stress distributions may cause multiple defects, such as springback. The springback is all the time one of the key factors restraining the bending quality and weakening the manufacturing efficiency [4]; as such, it is almost impossible to guarantee machining accuracy after primary processing. For this reason, it is essential to inspect the bent tubes and amend their geometric errors on the basis of inspection results, while at the same time calculating the springback of each arc. The springback of bent tubes contributes to in-process springback prediction and compensation, which can reduce the geometric error of tubes with present bending machine accuracy [5]. Therefore, the inspection of bent tubes is of great significance for automated production.

✉ Shaoli Liu
liushaoli@bit.edu.cn

[1] Laboratory of Digital Manufacturing, School of Mechanical Engineering, Beijing Institute of Technology, Beijing 100081, China

The methods used for tube measurements in the literature and in application can be divided into two broad categories: contact and non-contact methods (Fig. 1).

Contact methods utilize mechanical gauges [6] or three-coordinate measuring machines (CMMs) to inspect specific parts of tubes. When using a mechanical gauge, a mold is fabricated based on the shape of the tube. The tube can be classified into a good one or a bad one based on the fitness between the tube and the mold and cannot give the value of the geometric error. Moreover, the CMM uses probes directed to sample points on the tube surface for inspection of the tube; the geometric dimensions are determined from these sampling points. The automation of the contact method is low, making them more time-consuming, especially for tube with complex shapes and large dimensions.

Non-contact methods include scanning-based methods and vision-based methods. The scanning-based methods use laser scanning equipment to obtain point clouds on the tube surface, which are used to reconstruct a tube model and obtain the dimension data of every tube segment [7–10]. This method facilitates reconstruction of a three-dimensional (3D) model of the tube. However, technical deficiencies and human error may contribute to outlier samples during the scanning process. Moreover, the scanning data are noisy due to surface reflection. Thus, additional constraints are required to minimize noisy data. Also, the sample must be sufficiently large. For example, the scan of a tube with a 4-mm radius and 268-mm length in [8] contains 6005 sample points, which is better for obtaining robust results. However, as the calculation duration is proportional to the number of sample points, a large sample points require long computation times. For a complex tube, the optimization can take several minutes. Many ideas in the literature regarding tube inspection by machine vision methods are essentially obsolete in practice [11–15]. For example, Goulette et al. [11] used local estimates of the principal curvatures to divide a tube into line and arc segments; however, this approach was not capable of recognizing arc segments with small bending angles. Veldhuis et al. [12] used the bending angle of arc segments to reconstruct arcs; however, the bending angle caused by springback could not be determined and was only suitable for tubes with determinate shapes. Tangelder et al. [13, 15] and Vosselman et al. [14] matched the tube model with an image for model construction. Aubry et al. [16] attempted to resolve the two-dimensional (2D)/3D limitations of tube construction using a CAD model; however, the differences between the resulting tube construct and its model were not sufficiently accurate for tube inspection applications or reverse engineering of the tube.

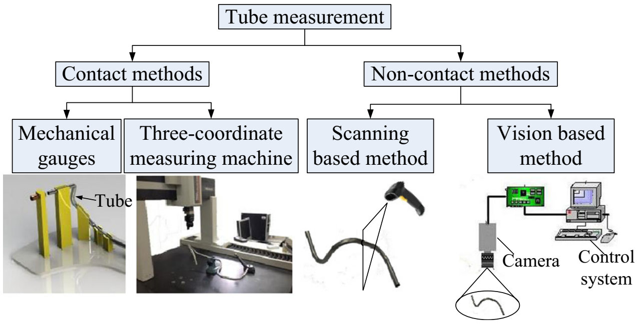

Fig. 1 The tube measurement methods

Moreover, there are some commercial systems in practice. They also have the disadvantages mentioned above. For example, Opton [17] reconstructed the tube model from the point clouds of the surface. Some general problems, outliers and noisy data, caused by reflective surfaces [18] should be tackled. Advanced Tubular and Tezet are arm systems [19, 20]. The dimensions of the tube must within the workspace of the arm. They recognize the line segments manually. The operator needs to sample points on the surface of every line segment. The efficiency will be reduced for a tube with complex shape and short line segments. Other similar commercial systems will not be introduced here.

Bosemann from Aicon Company published a paper on tube inspection systems in 1996 [21]. As the tubes are reconstructed by bend points, every bend point must be detected by at least two cameras and the displayed lengths of two line segments adjacent to the bend pint must be larger than 10 mm, However, this approach tends to be unstable and sensitive to the tube's pose, and for complex tubes in engineering, the short line segments are ubiquitous. The line segments do not satisfy the affine-invariant property; thus, some of the short line segments did not reach 10 mm in the image from any view. This has prevented the method from being applied in engineering. According to the product introduction of Aicon Company [22], the restrictions of the method (as cited in [21]) have been overcome. However, to our knowledge, no paper was published to explain the solution to the restrictions.

According to the analysis above, both contact and laser scanning methods can be time-consuming and inconvenient and are excessively dependent on human operation. Because of the development of digitization and automation in modern industry [23], along with the investigation that the measurement accuracy of aerospace tubes should be 0.2 mm, it is of great significance to develop a tube inspection method that is fast, accurate, and immune to artificial factors. Machine vision methods, advantageous for operational simplicity and high speed, can be used to obtain 3D information on objects by reconstructing the objects' models [24, 25] and may offer a good alternative for fast inspection of tubes.

However, there are still many problems to be solved. The general reconstruction process can be separated into three steps: key point extraction, matching, and reconstruction [26]. Extraction and matching determine the results of the reconstruction [27]. As the tube surface lack of texture and other characteristics which can provide strong cues to the 3D shape [28], it can be difficult to match common details between images, thus hindering reconstruction. Additionally, a significant question in tube inspection is how to accomplish the recognition and segmentation of line and arc segments of tubes, which can later be applied to calculate machining parameters [29, 30], specifically, YBC data, including lengths of line segments, bending angles of arcs, and angles between the surface normal vectors of two adjacent arcs. Moreover, springback can be obtained on the basis of measuring results of bending angles, which can be used to fix machining parameters. Due to the absence of affine invariance in linear and arc segments, especially when they are short, it is impossible to recognize these characteristics in images. For example, the bending angle of the arc in position 1 is 171° in Fig. 2 which is very close to a straight line; thus, it is recognized as a linear segment. Presently, there is still no effective method to recognize line and arc segments of tubes in the literature with machine vision. Thirdly, the necessity to process the tube surface as light reflection greatly affects the application and reduces measurement efficiency. Finally, it is hard to avoid the occlusion issue when taking images of complex tubes from only one direction. Figure 2 shows that the line segment in position 2 is occluded; thus, machine vision reconstruction provides limited information on the tube structure.

In order to solve the textureless issue, Chaibi et al. [50] defined the spheres, cylinders as the geometric primitives, and based on the bone contours in the biplannar X-rays to reconstruct the textureless lower limb. To deal with these engineering problems of the tube inspection mentioned above, we are inspired by Chaibi et al. [50], combining the geometric primitives and edges in the images, proposing a convenient and highly automated algorithm on the basis of multi-vision for tube reconstruction.

The transverse section of tubes is a circle with a constant diameter. The proposed algorithm first discretizes the tube on the basis of differentials, such that each segment can be regarded as a small cylinder which is the primitive of the tube. Then, the cylinder is reconstructed using a multi-vision technique and edges of the tube in all images. Finally, a tube model is created. The tube is mainly reconstructed based on the edges. So, the general industrial cameras can meet the requirements, without the need to use other latest sensors, such as depth sensors.

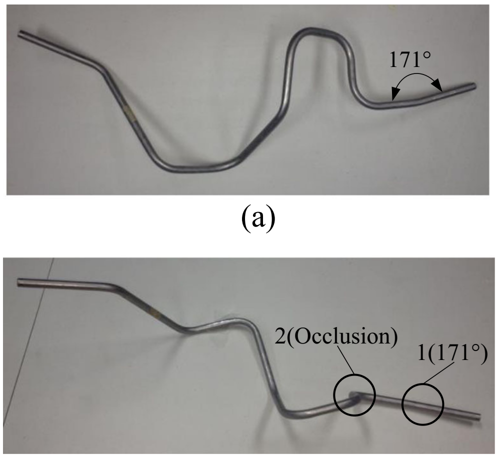

Fig. 2 The bending angle of the arc in position 1 is 171°, the line segment in position 2 is occluded

This method can solve the two main issues about the tube reconstruction, matching issue caused by the poor texture and the line and arc segments recognition.

(1) As we regard the tube as a composition of many small cylinders with a certain length, the matching accuracy is satisfactory within the length scale. Thus, the reconstruction method uses an epipolar line to solve the matching issue. In addition, this method reduces the calculation load and improves reconstruction speed significantly; only the cylinders are reconstructed as opposed to the reconstruction of point clouds of tubes.
(2) The pose of the cylinders are determined by matching their border with the tube edges in images of cameras in different views. The various matching errors can identify the line and arc segments. Moreover, the multi-vision technology not only ensures the reconstruction accuracy, but also avoids the occlusion issue of tubes with complex shapes. And the use of backlighting makes it easy to extract the edges of the tube with subpixel precision, minimizing issues associated with reflection.

Thus, the method described in this paper can be used to reconstruct a tube model and to inspect for geometric error of the tube through a comparison of reconstructed and CAD models. Also, a comparison of bending angles in the two models can be used to determine springback, allowing the machining parameters of the tube-bending machine to be optimized.

This study was performed on aerospace assembly tubes. The reconstruction accuracy was assessed by comparing the reconstruction model of this paper with the measurement results of a CMM. Section 2 gives an overview of the algorithm. In Section 3, an image-processing method is introduced for tube detection. Tube reconstruction is discussed in Section 4. Section 5 describes arc recognition and bend point calculations. Section 6 focuses on the reconstruction of the end points. Reconstruction accuracy and the inspection results are assessed in Section 7. Section 8 provides our conclusions.

2 Algorithm overview

Figure 3 shows the tube characteristics considered in this study. The tubes are made of alloys, such as nickel-titanium alloys, and bent by a bending machine. The arcs connecting two adjacent lines have a constant bend radius (*R*), which can be obtained from the bending machine's parameters. The tube cross-section is circular, and the tube diameter is constant.

(a) A typical tube

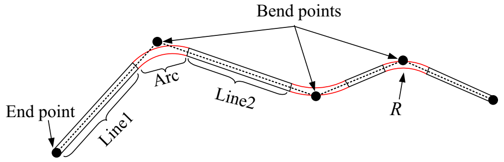

(b) The structure of a typical tube

Fig. 3 The characters of the tube in this paper

According to the specific description, the bend points, end points, and bend radius determine the geometry of the tube.

This paper proposes a method to reconstruct the tube by calculating the 3D coordinates of the bend points and end points. The algorithm flowchart is as follows.

The algorithm consists of three sections, as shown in Fig. 4.

(1) Tube detection. Backlight illumination [21] was used to minimize the influence of reflection from the tube's surface. The backlighting forms a strong contrast between the tube and the background. The difference in gray value can segment the tube region from the image, allowing the edges of the tube to be extracted with subpixel precision [31, 32].

(2) Initial model reconstruction. First, the reference image and the start location in it are determined to define the origin of the reconstruction. Second, an epipolar line is used to determine the start locations in other images. The positive direction along the *x*-axis in the world coordinate system (WCS) is defined as direction 1 and the negative direction in the *x*-axis is defined as direction 2, as shown in Fig. 5. Finally, small cylinders are reconstructed along directions 1 and 2, to the ends of the tube, to build the initial model.

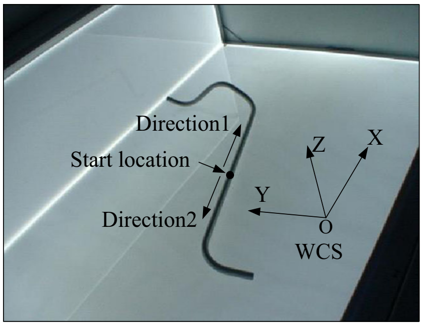

Fig. 5 Reconstruction directions

(3) Tube model reconstruction. In the process of reconstructing the small cylinders, the arcs and lines of the tube can be recognized by the matching error between the small cylinders and the subpixel-precision edges of the tube. The bend points can be calculated by intersecting two adjacent line segments. The directions of the tube's first and last line segments are obtained. Then, the end points of the tube can be determined by optimizing the length of the first and last line segments. The bend points and end points can then be used to reconstruct a model of the tube.

3 Tube detection

We extract the subpixel precision edge points to ensure the inspection accuracy [31, 32]. The backlighting minimizes the reflection and forms a strong contrast between the tube and the background which contribute to the extraction. The directional derivative of the edge points in the direction perpendicular to the edge is locally maximal. Figure 6 shows the strong contrast and the edge points. The extraction is typically based on a pixel grid; the distance between the edge points is approximately one pixel, on average.

Fig. 4 Algorithm flowchart

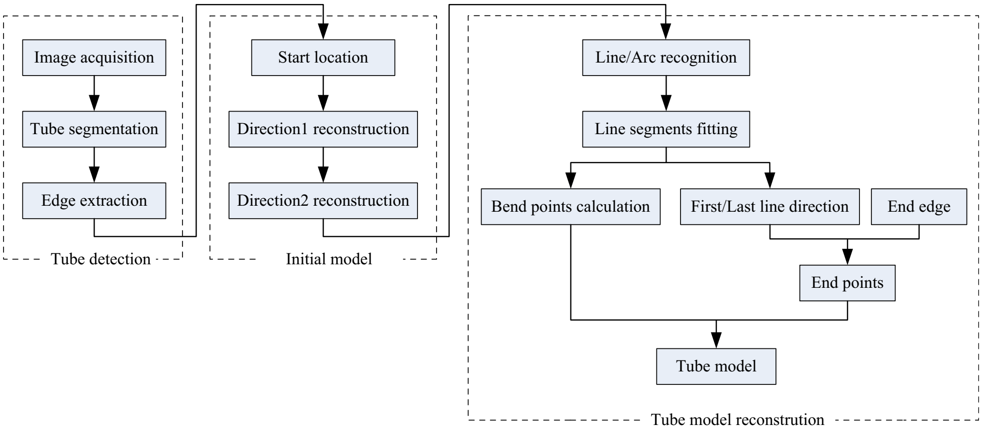

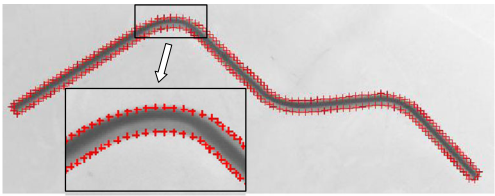

Fig. 6 The edge points of the tube

4 Initial model reconstruction

Regardless of how complex the shape of a tube, the proposed approach can be used to divide the tube into smaller, more manageable cylinders. These small cylinders are reconstructed using multi-vision and the edge points of the tube. The reconstruction method is as follows.

4.1 Camera calibration

Camera calibration of vision systems is to obtain the intrinsic and extrinsic parameter matrix. And its accuracy affects the 3D reconstruction results. This paper uses a bundle adjustment, widely used in photogrammetry and 3D reconstruction [26], for camera calibration.

Figure 7 shows the calibration process and the calibration equipment disposed in the photogrammetry space, including encoded points, an electro-optic (EO) device, and reference standards. Every camera has its own camera coordinate system (CCS). The WCS is determined by the EO device. There are five encoded points on the EO device and their relative positions are known. As every encoded point has a unique code value. The center encoded point is the origin. The Z-axis is vertical to the EO device plane and straight up. The X-axis can direct to any of the other four encoded points. The Y-axis is determined by the right-hand rule.

The Q_i is one encoded point in the space, its coordinates in the WCS and CCS are (X_w, Y_w, Z_w) and (X_c, Y_c, Z_c). Q_i can be projected on to the image by Eq. (1). The extrinsic parameters are the transformation between the WCS and the CCS ${}^{c}H_{w}$, which include a rotation matrix R and a translation vector T. The intrinsic parameters include the principal distance of the lens f, horizontal and vertical distance between two neighboring cells on the sensor d_y and d_x, column and row coordinate of the radial distortion center (u_0, v_0), and the distortion coefficient *kappa* [33].

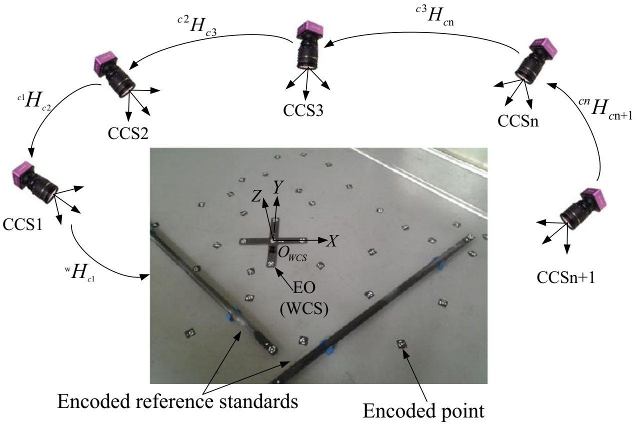

Fig. 7 Calibration process

$$\begin{cases} \begin{pmatrix} Xc \\ Yc \\ Zc \\ 1 \end{pmatrix} = {}^{c}H_{w} \begin{pmatrix} X_w \\ Y_w \\ Z_w \\ 1 \end{pmatrix} = \begin{pmatrix} R & T \\ 0 & 1 \end{pmatrix} \begin{pmatrix} X_w \\ Y_w \\ Z_w \\ 1 \end{pmatrix} \\ \begin{pmatrix} x \\ y \end{pmatrix} = \dfrac{f}{Zc} \begin{pmatrix} X_c \\ Y_c \end{pmatrix} \\ \begin{pmatrix} x' \\ y' \end{pmatrix} = \dfrac{2}{1+\sqrt{1-4 \times kappa \times (x^2+y^2)}} \begin{pmatrix} x \\ y \end{pmatrix} \\ \begin{pmatrix} u \\ v \end{pmatrix} = \begin{pmatrix} x' / dx \\ y' / dy \end{pmatrix} + \begin{pmatrix} u_0 \\ v_0 \end{pmatrix} \end{cases} \tag{1}$$

The intrinsic and extrinsic parameters can be calculated using the Levenberg–Marquardt algorithm [34–36] to minimize Eq. (2). In Eq. (2), n is the number of encoded points in an image, m is the number of cameras, q_{ij} is the image point of Q_i, and its projection point calculated by Eq. (1) is q'_{ij}. The transformation between different CCSs can be calculated by Eq. (3).

$$\sum_{j=1}^{m} \sum_{i=1}^{n} \left| \left| q_{ij} - q'_{ij} \right| \right|^2 \rightarrow \min \tag{2}$$

$${}^{ci}H_{cj} = {}^{ci}H_{w} \left({}^{cj}H_{w} \right)^{-1} \tag{3}$$

Here just introduced the general idea of the calibration process. This method has been widely used in the photogrammetry area for camera calibration and 3D reconstruction of target points [37, 38].

4.2 Start location determination

Current methods [39, 40] attempt to fit the end edge of the tube to an ellipse to calculate the position of the end point in images. This method can produce good results in cases where the edge of tube's end in the 2D image has a relatively complete ellipse. However, in industrial applications, the diameters of the tubes and viewing angles of cameras are different, which may affect the fitting of tube's end. For example, in the aerospace industry, the tube diameter is generally less than 15 mm. The diameters are smaller and the end edges are obscure which made the edge difficult to extract and fit into ellipse. Thus, it is a little difficult to determine the end points' positions. Therefore, we reconstructed the tube not from the end points; instead, the start location of the reconstruction is determined as follows.

We first determine the start location in the reference image. Then, find the matching points in other images by epipolar line. The matching points are the start locations in other images.

4.2.1 Reference image and start location determination

There is no specific requirement for the determination of the reference image. Any camera can be the reference if it captures the tube. Any position of the tube in the reference image can be the start location (except the end point, the reason is described above). For convenience, Fig. 8 shows a process for determining the start location. We can extract the skeleton of the tube region [41], and connect the two end pixels of the skeleton as. The perpendicular bisector of line L intersects the tube in the image. The intersection point is the start location.

4.2.2 Start locations in other images

According to the start location in the reference image, find the matching points in other images by using an epipolar line [42], as shown in Fig. 9. The matching points are the start locations in other images.

There are three cameras in Fig. 9. Camera O_1 is the reference. Its coordinate system is CCS_1. Image 1 is the reference image, and S_1 is the start location. Points p_1 and p_2 are on the line O_1S_1 in CCS_1. There coordinates in the WCS can be calculated with Eq. (4), ${}^{c1}H_w$ is the extrinsic parameter matrix of camera O_1.

$$\begin{pmatrix} X_w \\ Y_w \\ Z_w \\ 1 \end{pmatrix} = \left({}^{\mathrm{c}1}H_w\right)^{-1} \begin{pmatrix} X_c \\ Y_c \\ Z_c \\ 1 \end{pmatrix} \tag{4}$$

The epipolar line may result in matching ambiguity, as in Fig. 9 [43]. Points p_1 and p_2 can be projected onto image 2 to obtain line L_2'. Line L_2' intersects the tube; the intersection points are S_2 and S_2'. We use the trifocal tensor theory [44] to solve the matching ambiguity. Points p_1 and p_2 are projected onto image 3 to obtain line L_3. Line L_3 intersects the tube; the intersection points are S_3 and S_3'. The transformation between CCS_2 and CCS_3 can be calculated with Eq. (3). Point S3 in the image 3 corresponds to an epipolar line L_2 in image 2. Line L_2 intersects the tube with point S_2. Thus, points S_1, S_2, and S_3 are corresponding points. These three points are the start locations in the three images. This method can determine the start locations in all images.

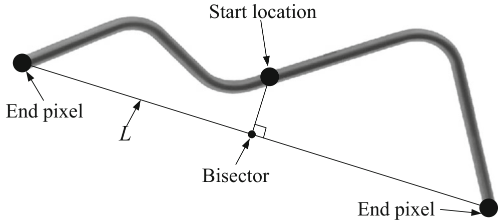

Fig. 8 Start location determination

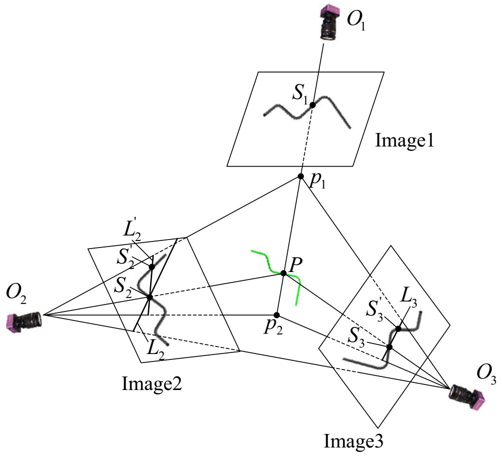

Fig. 9 Use the epipolar line to determine the matching position which is the start locations in different images

4.3 Small cylinder reconstruction

Reconstruction of the small cylinders uses a silhouette-based method, a reasonable alternative for recovering textureless objects [45, 50]. The details are as follows.

4.3.1 Reconstruction direction determination

WCS is a right-handed coordinate system, as shown in Fig. 5. The x- and y-axes are on the illumination surface. The z-axis is vertical to the surface and points straight up. For convenience, the angle between direction 1 and the positive direction of the x-axis is less than 90°. The two directions are shown in Fig. 5.

4.3.2 Small cylinder reconstruction

Reconstruction principle Figure 10 shows the reconstruction principle. Starting from the start position in all images, take a small section along direction 1. Image 4 does not capture the

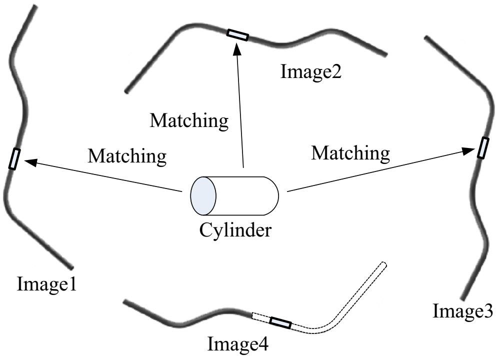

Fig. 10 The reconstruction principle

start location. So, image 4 does not participate in the reconstruction at the beginning. Build a small cylinder in the WCS and match the edge points in the image to the border of the cylinders to determine the pose of the small cylinders. Reconstruct the small cylinders with this method in directions 1 and 2. Image 4 will join in when the reconstructed small cylinders project onto image 4. All of the small cylinders comprise the initial model of the tube. Only when the length of the cylinder is short, we can discretize the tube into many small cylinders, referred to as primitives. You can decide the length of it by yourself. Our proposal is 4-mm long. Shorter cylinders affect the efficiency of the calculations and longer cylinders affect the recognition of short arcs. Here, a 4-mm-long section of the tube corresponded to approximately 10 pixels in the image. Thus, in the reconstruction process, every small section in the tube image is 10 pixels long.

The small cylinders are reconstructed by matching the border of the small cylinders with the edge points in the image, as shown in Fig. 11. The start location just needs to locate in the range of the small cylinder's length. The epipolar line can meet this requirement.

Implementation In Fig. 11, the pose of the small cylinders should be optimized to match the solid lines with the edge points. The small cylinder in the WCS needs to be projected onto every image repeatedly using Eq. (1). This made the computation involved to be extensive and time-consuming. The method shown in Fig. 12 improves computational efficiency. Here, the radius of the small cylinder is equal to the tube's radius. Thus, the center line is used to represent the small cylinder. A projection center, O_1 or O_2, and an edge point form a line L_j.

Ideally, the distance between the center line and L_j is equal to the radius. So, the center line can be determined by minimizing the Eq. (5). We use the Levenberg–Marquardt algorithm to solve it. In Eq. (5), i is the number of cameras, j is the number of L_j for a camera, d_{ij} is the distance between the center line and L_j in camera i, and D_1 is the matching error used for evaluating the fit.

$$D_1 = \min \sum_{i=1}^{n} \sum_{j=1}^{m} \left(d_{ij} - Radius \right) \tag{5}$$

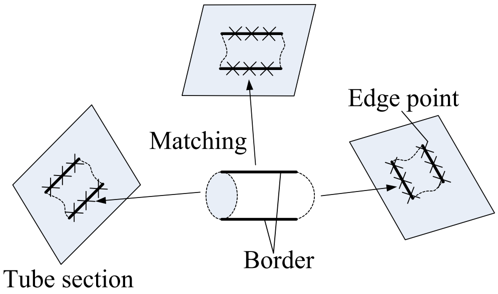

Fig. 11 The *black solid line* is the border of the cylinder

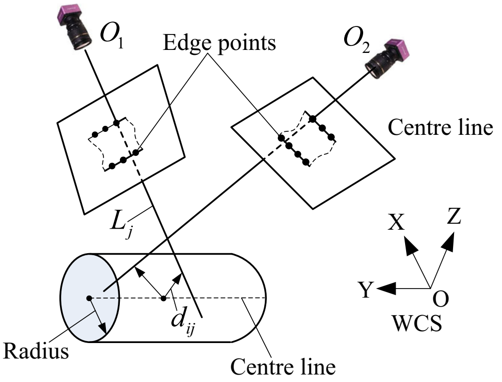

Fig. 12 The center line calculation of the cylinder

The method shown in Fig. 12 is used in Eq. (5) to calculate the center line via a least-squares calculation. The precision of the results improves as more cameras are added, each with different views.

4.3.3 Occlusion judgment

As shown in Fig. 13a, the tube is reconstructed along direction 1, for the reconstruction of the cylinder k, its center line is C_k, the direction of C_{k-1} is the initial value of C_k, which can be optimized by the method in Fig. 12. The C_k is projected on the image, the projection is c_k. As shown in Fig. 13b, the two lines c_{kL} and c_{kR} through the ends of c_k and perpendicular to c_k. The edges E_1 and E_2 between c_{kL} and c_{kR} are extracted. For non-occluded part, the distance between the middle points of E_1 and E_2 is d_1, which is equal to the tube diameter. As shown in Fig. 13c, for the occluded part, the distance is d_2, which is much bigger than d_1. We can define a threshold $T_O = 1$ pixels. Before the reconstruction of the cylinder k, for one image, if the distance between the two edges d is bigger than $(T_O + d_1)$, this part of tube in the image is occluded and it will not participate to reconstruct the cylinder k. As the reconstruction goes on, when d is less than $(T_O + d_1)$, this image can join the reconstruction again.

In this paper, as the cameras are in different locations, as shown in Fig. 13a, after the occlusion judgment, the occluded part of the tube can be reconstructed by other non-occluded images. So, the occlusion will not affect the results.

5 Arc recognition and bend point calculation

5.1 Arc recognition

Figure 14 shows the initial model of the tube in Fig. 6, composed of 193 small cylinders.

The matching error in Eq. (5) is small for the reconstruction of straight parts of the tube; it will be larger for reconstruction

Fig. 13 The occlusion judgment

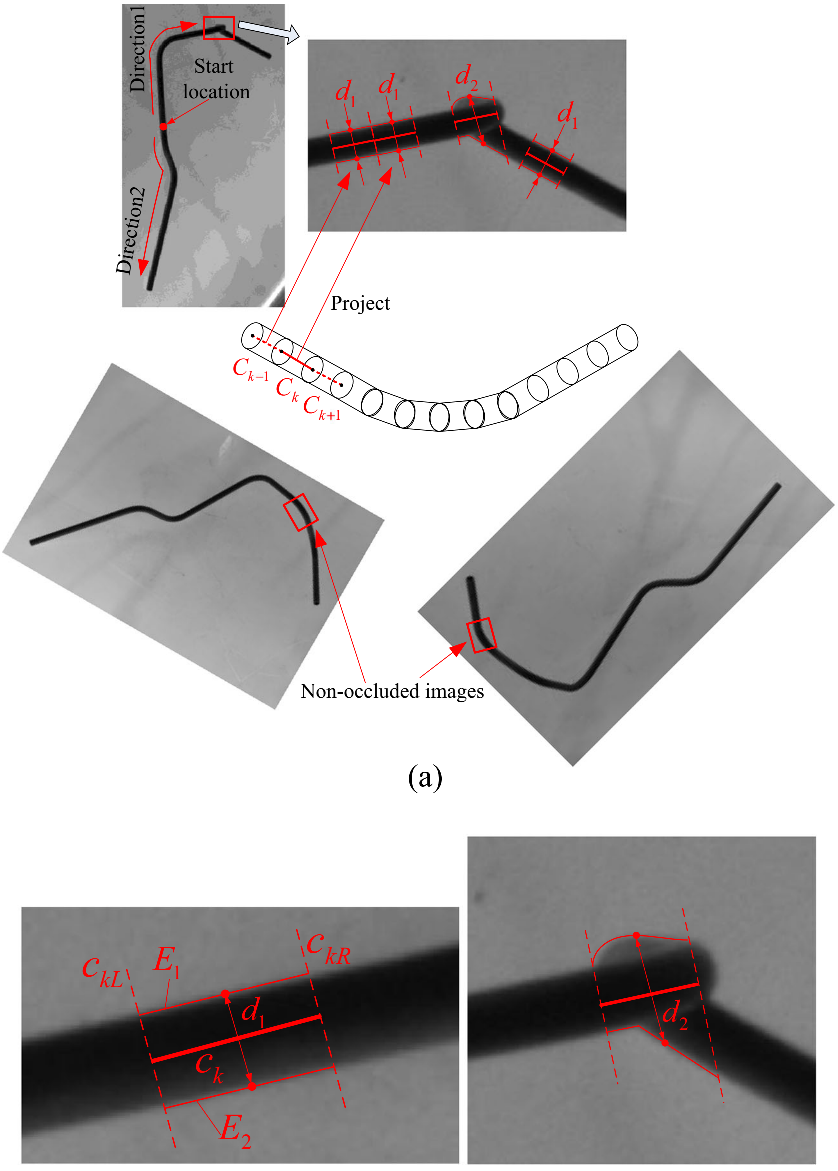

(a)

(b)

(c)

of the arcs. Figure 15 shows the matching error of the 193 small cylinders.

In Fig. 15, the cylinder index is shown as a function of the matching error. The small cylinders whose matching errors are higher than the average belong to the arcs. Small cylinders 43 to 72, 113 to 136, and 150 to 174 consist of three arcs; four line segments can also be recognized.

Experiments show that taking the average as the threshold can recognize 10° to 170° arcs. In practice, we can take the average as an initial threshold, and decrease with 1/10 the standard deviation as the interval. The output of the results is obtained when the number of recognized arcs is equal to the tube's arcs. Figure 16 shows another tube with six arcs: Fig. 16a is the matching error and Fig. 16b is the model. The angle of arc 1 in Fig. 16b is 8.2°. There is an obvious peak in the position of arc 1 in Fig. 16a. Thus, the matching error is sensitive to the arcs and can be used for arc recognition. We recognized 1° to 180° arcs within a suitable threshold.

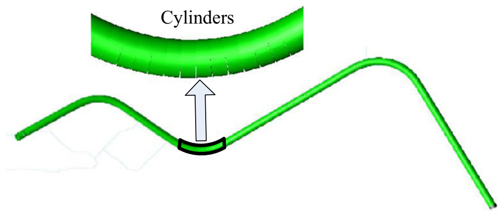

Fig. 14 The initial model

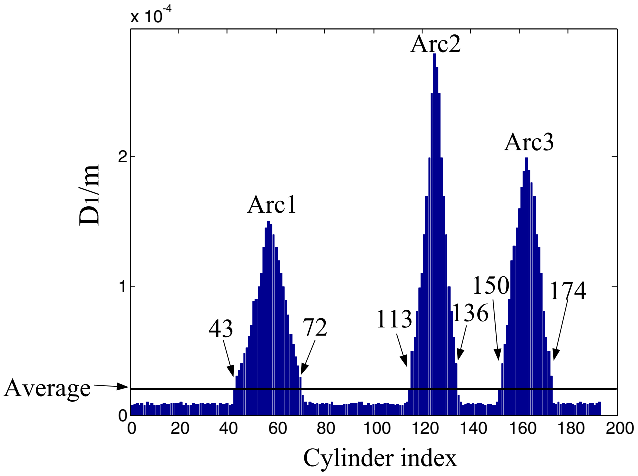

Fig. 15 The matching error

5.2 Bend point calculation

Based on the matching error, the cylinders belong to the straight and arc parts of the tube can be recognized, respectively. We fitted the end points of the cylinders belong to the straight part into line segment. As shown in Fig. 17, the line segment (Eq. (6)) can be calculated by minimizing $D_2=\sum_{i=1}^{n} \mathrm{t}_i$, t_i is the distance between the end points of the small cylinders and the line segment. In Eq. (6), (x_0, y_0, z_0) is a point on the line and (m, n, p) is a directional vector.

$$\frac{x-x_0}{m}=\frac{y-y_0}{n}=\frac{z-z_0}{p} \tag{6}$$

After fitting all of the line segments of the tube, the common vertical line of two adjacent line segments is calculated. The center point of the common vertical line is a bend point in the tube.

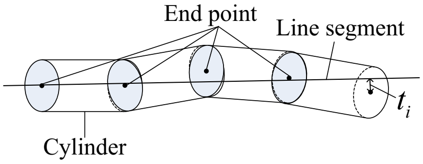

Fig. 17 Fitting the end points of the cylinders belong to the straight part into line segment

6 End point reconstruction

Up to this point, all of the bend points have been reconstructed, but the end points of the tube are unknown. The directions of the first and last line segments have been determined by fitting the cylinders belong to them. If the lengths of them are known, the end points of the tube can be reconstructed. Figure 18 shows the method of how to determine the length of the first and last line segments.

The first line segment of the tube is cylinder 1 and its length is length 1. Edge 2 is the projection of the end edge of the model. Edge 1 is the end edge of the tube in the image. Point p_i is an edge point, d_i is the distance between p_i and edge 2. Edge 1 and edge 2 are fit by optimizing the length of cylinder 1 (length 1 + △length). The end points are then determined using least-squares, as given by Eq. (7), with n as the number of edge points.

$$D_3=\min \sum_{i=1}^{n} d_i \tag{7}$$

All of the bend points and the end points have been reconstructed. These points determine the geometry of the tube. Next, we will verify the precision and reliability of the proposed algorithm.

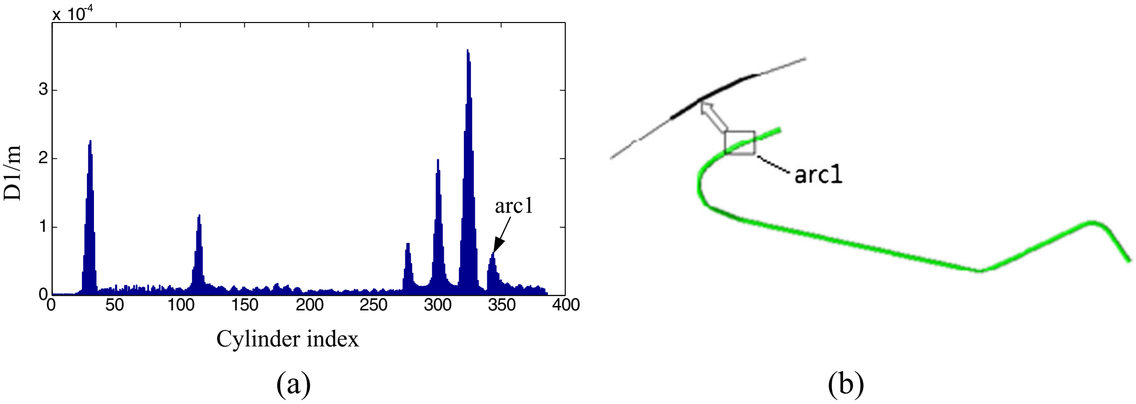

(a) (b)

Fig. 16 **a** The matching error; b the tube model

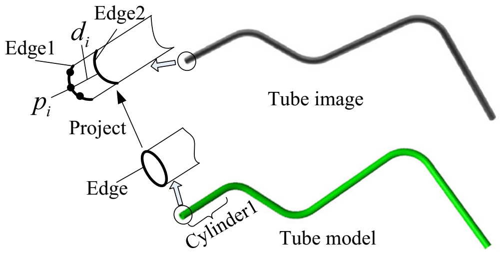

Fig. 18 End points reconstruction

7 Experiments and results

7.1 Multi-vision platform

We used the proposed algorithm to reconstruct different types of tubes. The precision of the CMM was 0.003 mm. The model reconstructed by the CMM was taken as the standard model of a tube (discussed in Section 7.2). The proposed algorithm can be examined by comparing the model reconstructed in this paper and the CMM.

This platform used 16 cameras in total, arranged as shown in Fig. 19. The industrial camera was a GuppyF-146B, produced by AVT Company (pixel size: 4.65 μm; resolution: 1388 × 1038; focal length: 8 mm). The distance between the upper eight cameras and the light plane was 2100 mm; the distance between the lower cameras and the light plane was 1900 mm. The size of the backlight source was 1850 × 1200 × 500 mm.

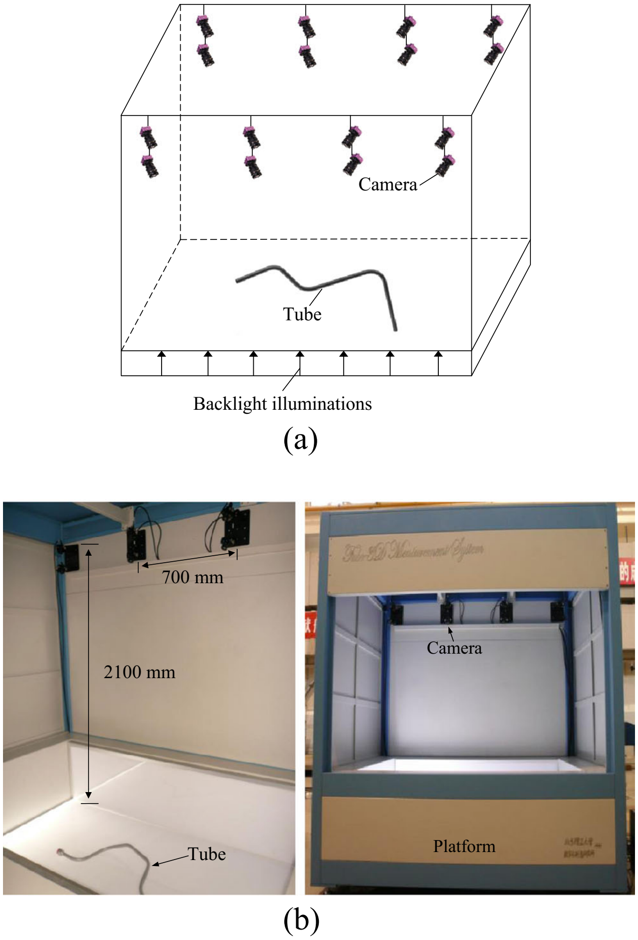

Fig. 19 Multi-vision platform

7.2 Standard model

The CMM can measure and reconstruct the geometry of the tube. The method is as follows. With the tube secured on the workbench, sample points were obtained from the surfaces of line segments via a probe; five sample points were obtained from each line segment. The sample points were then fit into cylinders using a least-squares technique [46]. The center line of the cylinders was used to calculate the bend points. The probe was then moved to the end of the tube to obtain additional sample points. This allowed fitting of the plane (Fig. 20), in which the end point corresponds to the intersection of the center line and the plane. The model was then constructed based on the bend points and end points.

YBC data can be used to represent the geometry of the tube. Figure 21 shows the standard model. Points p_1 and p_5 are the end points, and p_2 to p_4 are the bend points. The bending radius is R. The bend points and end points were used to calculate the YBC data.

C is the degree of bend, which can be calculated by Eq. (8).

$$C_i = \arccos \frac{p_i p_{i+1} \times p_{i+1} p_{i+2}}{|p_i p_{i+1}| \times |p_{i+1} p_{i+2}|}, i = 1, 2, 3 \tag{8}$$

Y is the distance between bends, which can be calculated by Eq. (9).

$$Y_i = |p_{i+1} p_{i+2}| - R \times tg\frac{C_i}{2} - R \times tg\frac{C_{i+1}}{2}, i = 1, 2, 3, 4 \tag{9}$$

B is the angles between the surface normal vectors of two adjacent bends. In Fig. 21b, one arc and its two adjacent lines constitute a plane. The normal of a plane can be described by Eq. (10):

$$N_i = p_i p_{i+1} \times p_{i+1} p_{i+2}, i = 1, 2, 3 \tag{10}$$

So, B can be given by Eq. (11):

$$B_j = \arccos \frac{N_j \times N_{j+1}}{|N_j| \times |N_{j+1}|}, j = 1, 2 \tag{11}$$

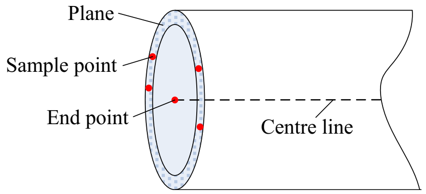

Fig. 20 Use the CMM to measure the end point

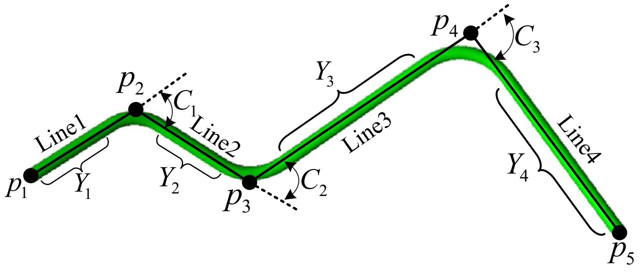

(a) The meaning of Y and C

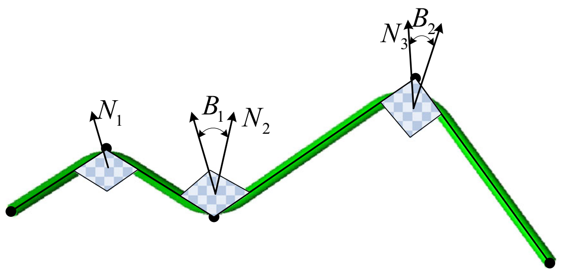

(b) The meaning of B

Fig. 21 The meaning of the YBC data

The sixth row in Table 1 is the YBC data of the standard model.

7.3 Reconstruction results

YBC data The tube shown in Fig. 6 was placed on a backlit measuring platform and moved repeatedly, 50 times, with different poses and positions. Then, the tube's model was reconstructed in each position and the YBC data were calculated. The first five rows in Table 1 showed five arbitrary sets of data from the results.

The seventh and ninth rows in Table 1 showed the average and standard deviation of the 50 sets of YBC data.

The precision of the measurement (Table 1) was obtained by subtracting the standard data from the average in Table 1. Based on the statistical results of Table 1, the precision was 0.17 mm and the standard deviation was 0.12 mm. Thus, the proposed approach provided good accuracy and stability.

The Cgk of the sheath deviation For measurement equipment, the measurement capability index, Cgk, is widely used to assess the measurement capability [47, 48]. It was calculated using Eq. (12).

$$\bar{x} = \frac{1}{n}\sum_{i=1}^{n} x_i$$

$$s = \sqrt{\frac{\sum_{i=1}^{n}\left(x_i - \bar{x}\right)^2}{n-1}} \qquad (12)$$

$$\mathrm{Cgk} = \frac{0.1 \times T - \bar{x}}{3 \times s}$$

In Eq. (12), n is the measurement times, x_i is a measurement result of a specific dimension, and T is the tolerance.

For tube inspection, use of the sheath deviation to examine the geometric error of the tube is also recommended in various directives, such as the American SAE J2551. The sheath deviation is the deviation between the standard and reconstructed models. Along and vertical to the tube at the end points and at the tangent points (starting and end points of the bend), the model has 10 sheath deviations, as shown in Fig. 22.

Figure 23 shows the method used to calculate the tangent points based on the bend points. Points A, C, and D are the bend points. Point B is the tangent point. R is the bend radius. The angle between line AC and line CD is θ. The point B can be calculated with Eq. (13).

$$B = C - \frac{\overrightarrow{|BC|}}{\overrightarrow{|AC|}} \times \overrightarrow{(AC)} \qquad (13)$$

We can fit the reconstructed model and the standard model to calculate the sheath deviation. Figure 24 shows the fitting method; d_j is the sheath deviation between the standard model and the reconstructed model. We minimized $D_4 = \sum_{j=1}^{n} d_j$ [29]

Table 1 Five arbitrary sets of data and statistical results of the 50 set of YBC data

No.	Y_1/mm	Y_2/mm	Y_3/mm	Y_4/mm	B_1/°	B_2/°	C_1/°	C_2/°	C_3/°
1	115.40	83.69	187.55	206.45	−156.37	163.84	59.00	66.19	88.62
2	115.41	83.70	187.52	206.46	−156.38	163.81	58.98	66.18	88.61
3	115.30	83.94	187.46	206.50	−156.35	163.86	58.96	66.14	88.64
4	115.25	83.86	187.46	206.51	−156.40	163.85	58.97	66.12	88.59
5	115.32	83.85	187.47	206.50	−156.36	163.89	58.93	66.11	88.62
Standard	115.27	83.94	187.43	206.39	−156.39	163.75	58.95	66.11	88.61
Average	115.30	83.77	187.47	206.49	−156.37	163.84	58.99	66.15	88.61
Precision	0.04	0.17	0.04	0.10	0.02	0.09	0.04	0.04	0
Stdev	0.06	0.12	0.04	0.05	0.01	0.04	0.03	0.03	0.02

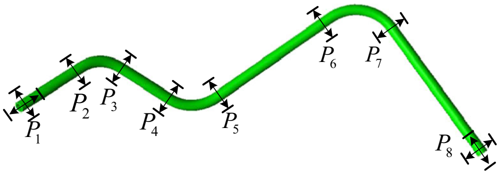

Fig. 22 Sheath tolerance

using a least-squares method to fit the two models, in which n is the number of sheath deviations.

So, we will calculate the Cgk of the sheath deviation of the tube shown in Fig. 6 to assess the reliability of the proposed algorithm. The acceptance criteria Cgk is 1.33 and the higher value are better. We reconstructed the tube 50 times and fit the reconstructed model with the standard model. Each sheath deviation d_j has 50 values. According to an investigation of actual aerospace tubes, the required sheath tolerance, T in Eq. (12), is 1 mm. The Cgk of the 10 sheath deviations is shown in Table 2.

According to the results in Table 2, min(Cgk) is 1.83, greater than the acceptance criterion of 1.33, indicating that 6210 erroneous results will occur in 1 million reconstructions; thus, the qualification rate is 99.9937%. The proposed algorithm showed good performance.

7.4 Other models

Figure 25 shows three tubes with different geometric dimensions. Figure 26(a1), (a2), (b), and (c) are the corresponding models.

In Fig. 26, the total length of the tube in (a1) is 804.43 mm, and the reconstruction time is 32 s; from (a2), we see that the angle of arc 3 is 4.1°. The total length of the tube in Fig. 26b is 1032.35 mm; the construction time is 62 s, the angle of arc 5 is 4.3°, and the length of line 89 is 5.3 mm. The total length of the tube in Fig. 26(c) is 1680.29 mm with 14 arcs, and the construction time is 113 s.

7.5 Discussion

Based on the experiments, the requirements of the operators are low and the time required minimal. The operators need only to place the tube within the measurement volume on the illumination table in any pose, and there is no need other operations; the inspection can be accomplished by the proposed system within 2 min automatically. So, it is immune to the artificial factors. In applications, platforms can be designed, according to the geometric dimensions of the tube. In Fig. 27, the platform consists of eight cameras; tubes can be inspected within 1100 mm. Tests showed that the precision of the reconstruction is sufficiently high if every part of the tube can be captured by five cameras. The details regarding the number and distribution of cameras and how they influence the reconstruction results should be examined further.

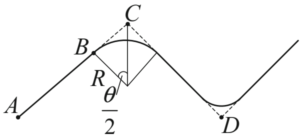

Fig. 23 Tangent points calculation

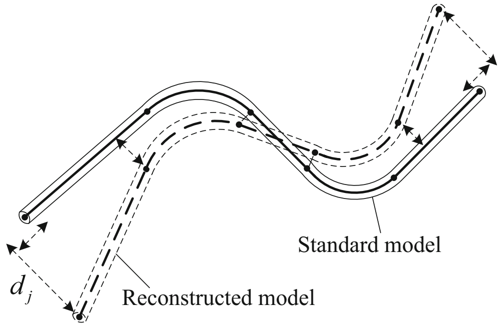

Fig. 24 Fit the reconstructed and CAD models

The proposed method is not dependent on the CAD model of the tube; thus, the method can be used for reverse engineering. In Fig. 28, for a tube with unknown geometry, the model can be reconstructed accurately and effectively, and the YBC data can be calculated for bending a new tube. Thus, the proposed approach offers a closed loop for tube manufacturing.

7.6 Future work

This paper suggests the need for further research in two areas.

(1) In this paper, the tube was reconstructed from the silhouette. The backlight illumination made it easier to extract sub-pixel edges. The brightness of the illumination and external light interference influences edge extraction and reconstruction results. Thus, some improvement is necessary to minimize these factors.

(2) The experiments were performed on a platform built by our group. The platform configuration allowed every backlit area to be captured by at least eight cameras. This provided sufficient precision; however, the number and distribution of cameras should be optimized.

Table 2 Cgk results calculated based on 50 reconstructions

No.	1	2	3	4	5	6	7	8	9	10
Cgk	1.83	2.25	5.32	9.74	8.54	4.19	5.63	4.25	2.16	1.85

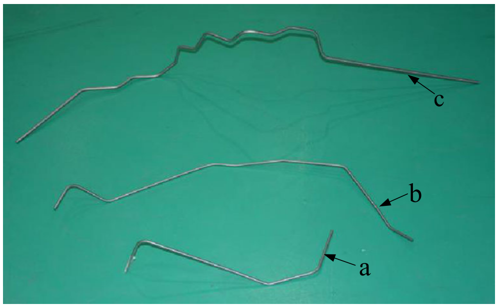

Fig. 25 Tube images

8 Conclusions

In industrial applications, the most studies include the mechanical gauges, CMM, scanning-based methods, and some commercial systems, are all based on artificial operations. Such as the CMM, the operator controls the probes directed to sample points on the tube surface for tube reconstruction; the geometric dimensions are determined from these sampling points. Therefore, the automation of the current methods is low, making them time-consuming. In addition, the artificial error may affect the results. Also the size and shape of the tube to be measured is limited by the workspace of CMM or mechanical arm.

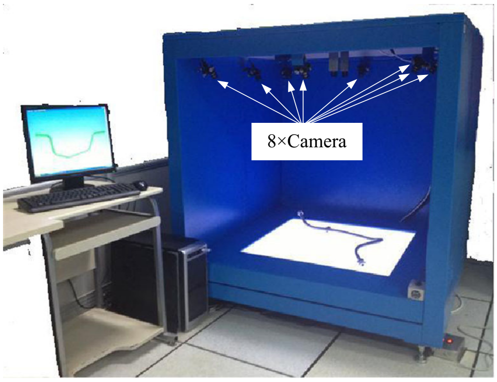

Fig. 27 Multi-vision platform

This paper proposes a multi-vision-based reconstruction method for tube inspection, which is much better than the previous. The method regards small cylinders as the primitives to reconstruct the tube. Each cylinder was reconstructed by matching its wire frame with the edge points in the images. The matching error made it easy to recognize the line and arc segments. The multi-vision technology solved the occlusion issue, and provided constraints from different directions, which ensured the reconstruction accuracy. The automation of the method made it immune to artificial factors. Therefore, for an inexperienced operator, he just need to put

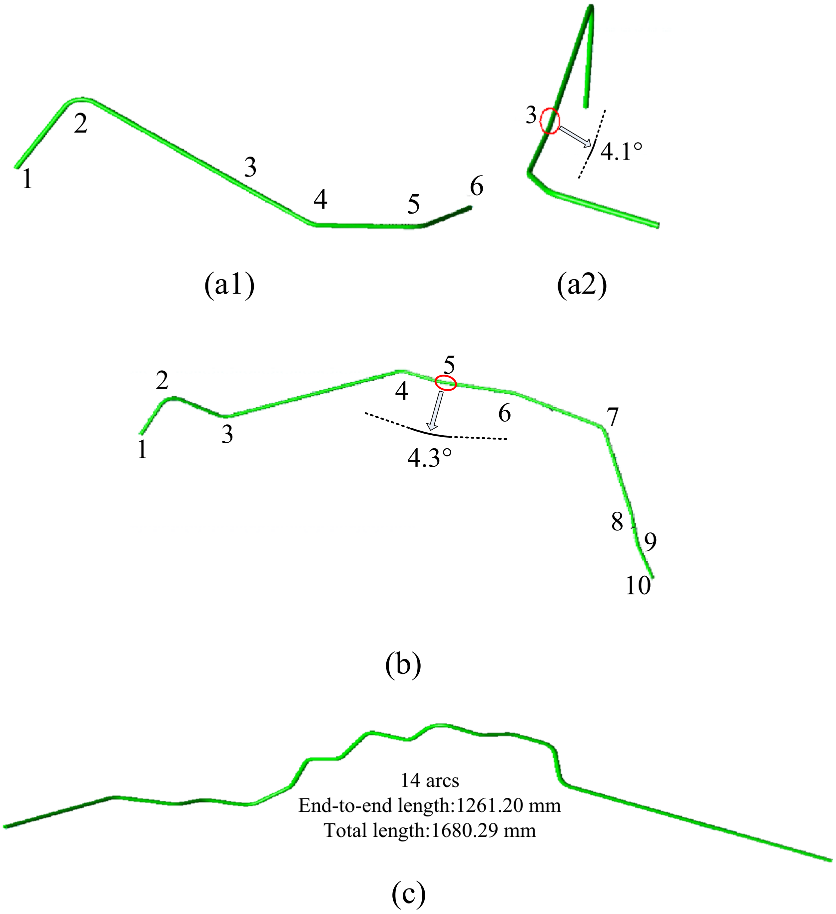

Fig. 26 Reconstructed tube models

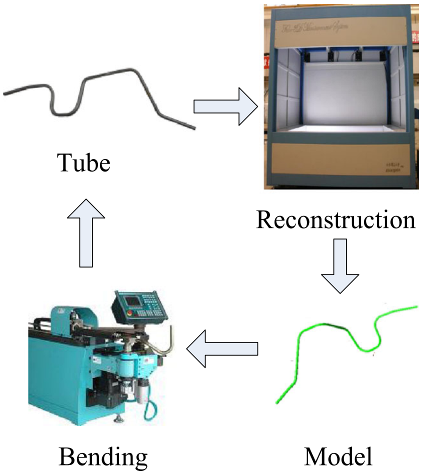

Fig. 28 Application in the reverse engineering

the tube on the illumination with any pose, the tube can be reconstructed and inspected automatically.

The proposed method is especially applicable to reconstruct the tubes with complex shapes and large dimensions. For a complex tube, the CMM and arm systems, such as Advanced Tubular and Tezet, the probe may not be able to get sample points on any part of the tube surface, caused the tube could not be reconstructed. For a large dimensional tube, as the automation of the most methods is low, the reconstruction time, include clamping and other artificial operations, may be more than half an hour. According to the experimental verification of the proposed method in this paper, for a tube with any dimension and shape within the measurement volume 1850 × 1200 × 500 mm, the reconstruction can be accomplished within 2 min. The reconstruction accuracy was 0.17 mm, allowing arc recognition of bending angles ranging from 1° to 180°. Besides, Cgk values of sheath deviation were larger than 1.33, indicating that the method is highly reliable. In general, the proposed method is simple to operate, immune to artificial factors, and can reconstruct the tubes with large dimensions and shapes efficiently and accurately. Moreover, the YBC data can be calculated based on the reconstruction model, the springback can be obtained from a comparison with bending angles of arc segments in the CAD model. This is advantageous for predicting and compensating for springback, which can reduce the geometric error of the tubes without increasing bending machine accuracy [49]. Thus, in the aerospace and other industrial fields, the method is of great significance in the automated production of tubes which can shorten the production cycle of the industrial vehicles.

One of the important contributions of this work is the development of a possible reconstruction method. The main features of an object can be loosely characterized by geometric primitives, such as points and segments in 3D, spheres, and cylinders. The multi-vision principle can be used to match and reconstruct primitives, which constitute the initial model of an object. Thus, the initial model is presented using descriptive parameters (e.g., sphere radius and sphere center coordinates). The initial model can be amended by optimizing the descriptive parameters, allowing 3D reconstruction based on the coherence of the initial model's projection with the contours in all of the images. The advantage is that the primitives can be reconstructed to automatically by multi-vision.

Our group will continue research on tube reconstruction and inspection to enhance reconstruction speed and accuracy for the inspection of tubes of arbitrary shapes and dimensions.

Acknowledgements This work has been funded by National Natural Science Foundation of China (NSFC, 51305031).

References

1. Liu Q, Wang C (2010) Pipe-assembly approach for aero-engines by modified particle swarm optimization. Assembly Auto 30(4):365–377. doi:10.1108/01445151011075825
2. Gibbon D, Ward J, Kay N (2000) The design, development and testing of a propulsion system for the snap-1 nanosatellite. Proc 14th Annual AIAA/USU Conference on Small Satellites (SSCOO-I-3), Logan, UT, Aug 2000.
3. Zhou C, Yin Y (2010) Pipe assembly planning algorithm by imitating human imaginal thinking. Assembly Auto 30(1):66–74. doi:10.1108/01445151011016082
4. He Y, Heng L, Zhiyong Z, Mei Z, Jing L, Guangjun L (2012) Advances and trends on tube bending forming technologies. Chin J Aeronaut 25(1):1–12. doi:10.1016/S1000-9361(11)60356-7
5. Guo XZ, Jin K, Wang H, Pei WJ, Ma FY, Tao J, Kim N (2016) Numerical simulations and experiments on fabricating bend pipes by push bending with local induction-heating process. Int J Adv Manuf Technol 84(9–12):2689–2695. doi:10.1007/s00170-015-7898-0
6. Feng YW, Thornton AC (2000) Tube production and assembly systems: the impact of compliance and variability on yield. ASME Design Automation Conference 2000, Baltimore.
7. Lee I-K, Kim KJ (2004) Shrinking: another method for surface reconstruction. In: GMP'04: Proceedings of the geometric modeling and processing, IEEE Computer Society: 259–266. doi: 10.1109/gmap.2004.1290047
8. Bauer U, Polthier K (2009) Generating parametric models of tubes from laser scans. Comput Aided Design 41(10):719–729. doi:10.1016/j.cad.2009.01.002
9. Kawashima K, Kanai S, Date H (2014) As-built modeling of piping system from terrestrial laser-scanned point clouds using normal-based region growing. J Comput Des Eng 1(1):13–26. doi:10.7315/JCDE.2014.002
10. Son H, Bosche F, Kim C (2015) As-built data acquisition and its use in production monitoring and automated layout of civil infrastructure: a survey. Adv Eng Inform 29(2):172–183. doi:10.1016/j.aei.2015.01.009
11. Goulette F (1997) Automatic cad modeling of industrial pipes from range images. Proc Int'l Conf 3D Digital Imaging and Modeling. Los Alamitos, CA: 229-233. doi:10.1109/IM.1997.603870
12. Veldhuis H, Vosselman G (1998) The 3D reconstruction of straight and curved pipes using digital line photogrammetry. ISPRS-J Photogramm Remote Sens 53(1):6–16. doi:10.1016/S0924-2716(97)00031-2
13. Tangelder JWH, Vosselman G, Heuvel FAVD (2000) Object-oriented measurement of pipe systems using edge matching and

csg models with constraints. Int Arch Photogramm Remote Sens XXXIII(Supplement B5):132–139

14. Vosselman G, Tangelder JWH (2000) 3D reconstruction of industrial installations by constrained fitting of cad models to images. Mustererkennug, G. Sommer, N. Kruger, Ch. Perwass (Eds.), Informatik aktuell, Springer Verlag: 185-92. doi:10.1007/978-3-642-59802-9_36
15. Tangelder JWH, Ermes P, Vosselman G, Heuvel FAVD (2003) CAD-based photogrammetry for reverse engineering of industrial installations. Computer Aided Civ Inf 18(4):264–274. doi:10.1111/1467-8667.00316
16. Aubry M, Maturana D, Efros AA, Rusell BC, Sivic J (2014) Seeing 3d chairs: exemplar part-based 2d-3d alignment using a large dataset of CAD models. In: 2014 I.E. Conference on Computer Vision and Pattern Recognition:3762–3769
17. Opton. Available at: http://www.opton.co.jp/en/products/3d/pipe3d-profiler-series/. (Accessed 20 December, 2015)
18. Fisher RB (2004) Applying knowledge to reverse engineering problems. Comput Aided Design 36(6):501–510. doi:10.1016/S0010-4485(03)00158-1
19. Advanced tubular. Available at: http://www.advancedtubular.com/vtube-laser.htm (Accessed 20 December, 2015)
20. Tezet. Available at: http://www.tezet.com. (Accessed 20 December, 2015)
21. Bosemann W (1996) The optical tube measurement system olm-photogrammetric methods used for industrial and process control. Int Arch Photogramm Remote Sens XXXL(part b5):55–58
22. Aicon. Available at http://aicon3d.com/products/tubeinspect-products/tubeinspect/technical-details.html (Accessed 20 February, 2016)
23. Brettel M, Friederichsen N, Keller M, Rosenberg M (2014) How virtualization, decentralization and network building change the manufacturing landscape: an industry 4.0 perspective. Int J Mech Aerosp Ind Mechatron Manufac Eng 8(1):37–44
24. Fiorenzo F, Domenico M (2014) The evolution of large-scale dimensional metrology from the perspective of scientific articles and patents. Int J Adv Manuf Technol 70(5):887–909. doi:10.1007/s00170-013-5317-y
25. Luhmann T (2010) Close range photogrammetry for industrial applications. ISPRS-J Photogramm Remote Sens 65(6):558–569. doi:10.1016/j.isprsjprs.2010.06.003
26. Ahmadabadian AH, Robson S, Boehm J, Shortis M, Wenzel K, Fritsch D (2013) A comparison of dense matching algorithms for scaled surface reconstruction using stereo camera rigs. ISPRS-J Photogramm Remote Sens 78:157–167. doi:10.1016/j.isprsjprs.2013.01.015
27. Remondino F, Spera MG, Nocerino E, Menna F, Nex F (2014) State of the art in high density image matching. Photogramm Rec 29(146):144–166. doi:10.1111/phor.12063
28. David CK (2001) Contour into texture: information content of surface contours and texture flow. J Opt Soc Am A 18(1):12–35. doi:10.1364/JOSAA.18.000012
29. Lou HZ, Stelson KA (2001) Three-dimensional tube geometry control for rotary draw tube bending, part 2: statistical tube tolerance analysis and adaptive bend correction. J Manuf Sci E-T Asme 123:266–271
30. Ding G, Jiang L, Qin S, Zhu S, Ma S (2012) Computer-integrated manufacturing system for tube bending. Int J Comput Integ M 25(11):1059–1068. doi:10.1080/0951192X.2012.684710
31. Shrivakshan GT, Chandrasekar C (2012) A comparison of various edge detection techniques used in image processing. Int J Comput Sci Issues 9(4):269–276
32. Chen NQ, Wang JJ, Yu LA, Su CY (2014) Sub-pixel edge detection of led probes based on canny edge detection and iterative curve fitting. International Symposium on Computer, Consumer and Control (IS3C):131-134.doi:10.1109/IS3C.2014.45
33. Fitzgibbon AW (2001) Simultaneous linear estimation of multiple view geometry and lens distortion. In: Proceedings of IEEE Conference on CVPR:125–132.doi:10.1109/CVPR.2001.990465
34. Furukawa Y, Ponce J (2008) Accurate camera calibration from multi-view stereo and bundle adjustment. Computer Vision and Pattern Recognition, Anchorage, Alaska, USA,:1-8.doi:10.1109/CVPR.2008.4587681
35. Triggs B, McLauchlan PF, Hartley RI, Fitzgibbon AW (2002) Bundle adjustment-a modern synthesis. Vision algorithms: theory and practice. Volume 1883 of the series Lecture Notes in Computer Science: 298-372.
36. Madsen K, Nielsen HB, Tingleff O (2004) Methods for non-linear least squares problems. 2nd Edition, April 2004.
37. Miroslaw K, Jerzy W, Filip P (2013) Application of reverse engineering for identification of damage and support the reparation of the vehicles. J KONES Powertrain Transp 20(4):155–161
38. Bosemann W (2005) Advances in photogrammetric measurement solutions. Comput Ind 56(8–9):886–893. doi:10.1016/j.compind.2005.05.014
39. Wade P, Moran D, Graham J, Jackson CB (1997) Robust and accurate 3d measurement of formed tube using trinocular stereo vision. The British Machine Vision Conference. BMVC, Essex, UK: 1-10.
40. Bergamasco F, Cosmo L, Albareli A, Torsello A (2012) A robust multi-camera 3d ellipse fitting for contactless measurements.2012 Second Joint 3DIM/3DPVT Conference: 3D Imaging, Modeling, Processing, Visualization & Transmission: 168–175. doi:10.1109/3dimpvt.2012.22
41. Ogniewicz RL (1994) Skeleton-space: a multiscale shape description combining region and boundary information, Proc of IEEE Comp Soc Conf Comp Vis Pattern Recogn: 746–751.doi:10.1109/CVPR.1994.323891
42. Zoran M, Najdan V, Marko M, Bojan B (2014) New hybrid vision-based control approach for automated guided vehicles. Int J Adv Manuf Technol 66(1):231–249. doi:10.1016/0004-3702(95)00022-4
43. Zhang Z, Deriche R, Faugeras O (1995) A robust technique for matching two uncalibrated images through the recovery of the unknown epipolar geometry. Artif Intell 78(1–2):87–119
44. Torr PHS, Zisserman A (1997) Robust parameterization and computation of the trifocal tensor. Image Vis Comput 15(8):591–605. doi:10.1016/S0262-8856(97)00010-3
45. Kolev K, Brox T, Cremers D (2012) Fast joint estimation of silhouettes and dense 3d geometry from multiple images. IEEE T Pattern Anal 34(3):493–505. doi:10.1109/TPAMI.2011.150
46. Lukacs G, Martin R, Marshall D (1998) Faithful least-squares fitting of spheres, cylinders, cones and tori for reliable segmentation. In 5th European Conference on Computer Vision, Lecture Notes in Computer Science, Vol. 1406, Springer: 671-686. doi:10.1007/bfb0055697
47. Shojaei R, Sohrabi M, Amjadi MA (2010) Statistical measurement system analysis of ruston TA1750 gas turbine 1st stage nozzle. Adv Math Comput Meth: 29–33
48. Rahmati SHA, Amalnick MS (2015) Fuzzy gauge capability (Cg and Cgk) through buckley approach. Int J Mech Aerosp Ind Mechatron Manuf Eng 9(8):1467–1470
49. Li H, Yang H, Song FF, Zhang M, Li GJ (2012) Springback characterization and behaviors of high-strengh ti-3ai-2.5v tube in cold rotary draw bending. J Mater Process Tech 212(9):1973–1987. doi:10.1016/j.jmatprotec.2012.04.022
50. Chaibi Y, Cresson T, Aubert B, Hausselle J, Neyret P, Hauger O, de Guise JA, Skalli W (2012) Fast 3d reconstruction of the lower limb using a parametric model and statistical inferences and clinical measurements calculation from biplanar x-rays. Comput Method Biomecc 15(5):457–466. doi:10.1080/10255842.2010.540758